Electrochimica Acta 107 (2013) 664–674

Contents lists available at ScienceDirect

Electrochimica Acta

journal homepage: www.elsevier.com/locate/electacta

Heating strategies for Li-ion batteries operated from subzero temperatures

Yan Ji[a], Chao Yang Wang[a,b,*]

[a] Electrochemical Engine Center (ECEC), Department of Mechanical and Nuclear Engineering, The Pennsylvania State University, University Park, PA 16802, USA
[b] EC Power, State College, PA 16803, USA

ARTICLE INFO

Article history:
Received 7 January 2013
Received in revised form 22 March 2013
Accepted 23 March 2013
Available online 6 April 2013

Keywords:
Lithium-ion batteries
Modeling
Heating
Low temperature
Thermal management

ABSTRACT

Electric vehicles (EVs) suffer from significant driving range loss in subzero temperature environments due to reduced energy and power capability of Li-ion batteries as well as severe battery degradation due to Li plating. Preheating batteries to room temperature is an essential function of an effective battery management system. The present study employs an electrochemical–thermal coupled model to simulate, for the first time, the process of heating Li-ion batteries from subzero temperatures. Three heating strategies are proposed and compared using battery power, namely self-internal heating, convective heating and mutual pulse heating, as well as one strategy (AC heating) using external power. Their advantages and disadvantages are discussed in terms of capacity loss, heating time, system durability, and cost. For heating using battery power, model predictions reveal that Li-ion batteries can be heated from −20 °C to 20 °C at the expense of only 5% battery capacity loss using mutual pulse heating with high-efficiency dc–dc converter, implying considerable potential for improved driving range of EVs in cold weather conditions. Moreover, the heating time can be reduced to within 2 min by increasing cell output power using convective heating and mutual pulse heating. For external power heating, high frequency AC signal with large amplitude is a preferred choice, offering both high heating power and improved battery cycle life.

1. Introduction

Electric drive vehicles are a promising technology for critical reductions of both greenhouse gas emissions and dependence on foreign oils. The market share of plug-in hybrid electric vehicles (PHEV) and pure electric vehicles (EVs) has increased significantly in recent years. Despite offering advantages of energy efficiency and low environmental impact, market penetration of EVs is limited by relatively short driving range. Compared to gasoline vehicles with over 300 mile range before refueling, EVs can achieve only 100–150 miles before recharging. Furthermore, EV driving range depends greatly on ambient conditions. For instance, driving range of the 2012 Nissan Leaf approaches 138 miles at the ideal condition, but drops substantially to 63 miles in cold weather at −10 °C [1].

At subzero temperatures, in spite of additional energy consumed for cabin heating, the range limiting factor is closely related to significantly reduced energy and power capability of Li-ion batteries [2,3], as well as capacity fade due to lithium plating upon charging [4,5]. Fundamentally, the poor performance of Li-ion batteries at subzero temperatures arises from sluggish kinetics of charge transfer [6,7], low electrolyte conductivity [8,9] and reduced solid-state Li diffusivity [6,10]. While these limitations might be alleviated by finding more suitable electrolyte and active materials, an alternative is the system approach based on battery thermal management to quickly pre-heat batteries to normal operation temperature before use [11,12]. Since the kinetic and transport processes are highly temperature dependent, cell performance will quickly recover during warm up.

The poor performance of Li-ion cells at subzero temperatures implies significantly increased internal resistance. A tenfold increase in resistance relative to room temperature has been measured from commercial cells at −20 °C [13]. The high internal resistance reduces cell energy and power capability, yet is beneficial to cell warm up because of more internal heat generation, which can induce remarkable temperature rise and thereby restore cell performance. During the operation of Li-ion cells at subzero temperatures, there exists strong interplay between electrochemical and thermal processes. On the one hand, the heat generated from electrochemical processes, along with heat dissipation to the ambient environment, dictates cell temperature evolution. On the other hand, the cell temperature affects the electrochemical processes via highly temperature-dependent kinetic and transport properties.

* Corresponding author at: Electrochemical Engine Center (ECEC), Department of Mechanical and Nuclear Engineering, The Pennsylvania State University, University Park, PA 16802, USA. Tel.: +1 814 863 4762; fax: +1 814 863 4848.
E-mail address: cxw31@psu.edu (C.Y. Wang).

0013-4686/$ – see front matter © 2013 Elsevier Ltd. All rights reserved.
http://dx.doi.org/10.1016/j.electacta.2013.03.147

Understanding this interplay is key to prediction of cell behavior and development of innovative heating strategies for Li-ion cells in subzero environments.

A literature survey on battery thermal management reveals that most prior studies focused on cooling issues. In contrast, studies on battery heating strategies are scarce. Cooling received attention because battery aging and safety issues at high operating temperatures are of great concern for previously launched HEVs, where the internal combustion engine is the primary power source. With the recent introduction of EVs to the automotive market, vehicle performance relies more on batteries. Battery performance in cold climates has thus become a limiting factor for driving range, and efficient heating strategies have become a pressing need.

Pesaran et al. [12,14] studied preheating techniques in cold climates including core heating, jacket heating and fluid heating. These heating strategies were simulated using thermal finite element models for heat transfer. Battery temperature evolutions of different heating techniques were compared. For core heating, the internal heating power was specified as a constant or linear variation with time, instead of being calculated from electrochemical processes. Their model simulated the heating process as a pure heat transfer problem, and therefore lacked the ability to predict nonlinear electrochemical–thermal coupling behaviors. Use of an electrochemical–thermal coupled model is more appropriate to study heating strategies at subzero temperatures where cell internal heating is significant. Additionally, external heating using alternating current was experimentally studied by Stuart and Hande [15]. AC signals of 60 Hz and 20 kHz with different amplitudes were tested on lead acid batteries and nickel metal hydride batteries, respectively. It was found that the heating process sped up as the signal amplitude was increased. However, the effect of signal frequency on heating time and battery cycle life was not studied. Fundamental understanding of battery behaviors under AC signals is still to be revealed.

While a few heating strategies have been proposed, it remains unclear which strategy is preferable and how much room remains for further improvement. To answer these questions, in this work, we introduce four criteria for heating strategy evaluation: (1) electrical energy consumption in terms of battery capacity, or equivalently, in terms of driving range of EVs, (2) heating time, (3) effect of heating operation on system durability including battery cycle life, and (4) system cost. Understanding the theoretical limits of these criteria will help manufacturers select, optimize and implement viable heating strategies.

This work makes an attempt to exploit electrochemical–thermal interactions. Various heating strategies are proposed and compared using the four criteria cited above. For EVs, battery pack is the only onboard power plant and thus the primary source of heating energy. Whenever access to electric power is available, consumers can choose external power without sacrificing battery capacity. This paper examines heating strategies involving use of both battery and external power.

2. Theory

2.1. Description of the system

For simplicity but without losing generality, 18650 cells of 2.2 Ah capacity are studied here, instead of a whole battery pack. This provides a good approximation when cell-to-cell temperature difference across the battery pack is sufficiently small and when state of charge (SOC) and state of health (SOH) are uniform.

Design parameters of the 18650 cells are listed in Table 1. The anode consists of 95.5% graphite, 1.5% Super P carbon black and 3% PVDF (by weight), with anode thickness of 80 μm. The cathode compositions are generally 94% NCM ($LiNi_{1/3}Co_{1/3}Mn_{1/3}O_2$), 3% Super P carbon black and 3% PVDF. Thickness of this cathode is 78 μm. The cell has an N/P (negative to positive electrode) ratio of 1.15 and electrode coating area of 640 cm^2. Active material loading in the cathode is 3.9 mAh cm^{-2}. Using material balance, the porosities of anode and cathode are calculated as 0.26 and 0.28 respectively. Separator of 20 μm thickness and 0.46 porosity is used. The electrolyte is 1.2 M $LiPF_6$ in a mixture of PC, EC and DMC (10:27:63 by volume).

Table 1
Design parameters of 18650 cells.

Parameters	Anode (graphite)	Separator	Cathode (NCM)
Thickness (μm)	81	20	78
Porosity	0.26	0.46	0.28
Loading (mAh cm^{-2})	4.5	–	3.9
Electrolyte concentration (mol dm^{-3})	1.2		
Particle radius (μm)	10	–	5

The ambient temperature is fixed at −20 °C, which is also the cell's starting temperature. Heating strategies are employed to heat the cell to 20 °C for performance boost. Adiabatic condition on cell surfaces is assumed whenever convective heat transfer is not used. Unless explicitly specified, the initial voltage of the cell is 3.8 V, corresponding to 64%SOC.

2.2. Model description

The present work uses the electrochemical–thermal (ECT) coupled model described in detail by Gu and Wang [16], Srinivasan and Wang [17], Luo and Wang [18], and Ji et al. [19]. The ECT model builds on the conventional electrochemical model of Newman and co-workers [20–22] but accounts for the tight coupling between electrochemical and thermal dynamics and is essential for the modeling of thermally sensitive batteries such as Li-ion cells. A set of the governing equations are given in the appendix. Relevant electrochemical properties are listed in Table 2. Use of the ECT model requires a comprehensive database of temperature- and concentration-dependent material properties. To this end, more than one hundred thousand coin cells have been built and tested to acquire material properties under a wide range of temperatures and compositions in a CAEBAT (Computer-Aided Engineering for Batteries) project led by EC Power and sponsored by U.S. Department of Energy [23]. Based on this comprehensive material database, the electrochemical model has been coupled with heat transfer and validated against the above described 18650 cells at various rates and temperatures [19]. The modeling results are compared with experimental data in terms of both voltage and temperature. Good agreement was obtained from 0.1 C to 4.6 C rate and from −20 °C to 45 °C ambient temperature. The experimentally validated model is used to investigate heating strategies in the present study.

3. Results and discussion

3.1. Heating strategies using battery power

In this section, three heating strategies are proposed and evaluated, taking full advantage of the fact that internal heat generation is greatly enhanced at low temperatures. These strategies include self-internal heating, convective heating and mutual pulse heating, as shown in Fig. 1. All of them have resistance heating effect included.

3.1.1. Self-internal heating

The self-internal heating strategy heats the cell through internal resistance solely. For rapid heating, high rate operation is desirable, creating a high overpotential. Charging operation should be

Table 2
Electrochemical properties.

Properties	Graphite (Li_xC_6)	$Li_yNi_{1/3}Mn_{1/3}Co_{1/3}O_2$
Exchange current density i_0 ($A\,m^{-2}$)	12 [17] ($x = 0.5$)	2[b] ($y = 0.5$)
Activation energy of i_0 ($kJ\,mol^{-1}$)	68 [24]	50 [24]
Charge transfer coefficient $\alpha_a\ \alpha_c$	0.5 0.5[a]	0.5 0.5[a]
Film resistance R_f ($\Omega\,cm^{-2}$)	10[b]	10[b]
Activation energy of R_f ($kJ\,mol^{-1}$)	50[b]	50[b]
Solid state diffusivity D_s ($m^2\,s^{-1}$)	$1.6 \times 10^{-14}(1.5 - x)^{1.5}$ [25]	3×10^{-14} [25,26]
Activation energy of D_s ($kJ\,mol^{-1}$)	30 [27]	30[a]
Contact resistance ($\Omega\,cm^{-2}$)	6[b]	
Open circuit potential (V vs. Li/Li^+)	$U_1(x)$[c] [28]	$U_2(y)$[c] [29]
Reversible heat	Refer to Reynier et al. [30]	Refer to Lu et al. [31]
Electrolyte properties	Data from Valoen and Reimers [32] with adjustment [19]	

[a] Assumed values.
[b] Extracted from model-experimental comparison
[c] Open circuit potential data has been fitted to empirical equations:

$$U_1(x) = 0.1493 + 0.8493e^{-61.79x} + 0.3824e^{-665.8x} - e^{39.42x-41.92} - 0.03131\arctan(25.59x - 4.099) - 0.009434\arctan(32.49x - 15.74) \quad (0 \le x \le 1)$$

$$U_2(y) = -10.72y^4 + 23.88y^3 - 16.77y^2 + 2.595y + 4.563 \quad (0.3 \le y \le 1)$$

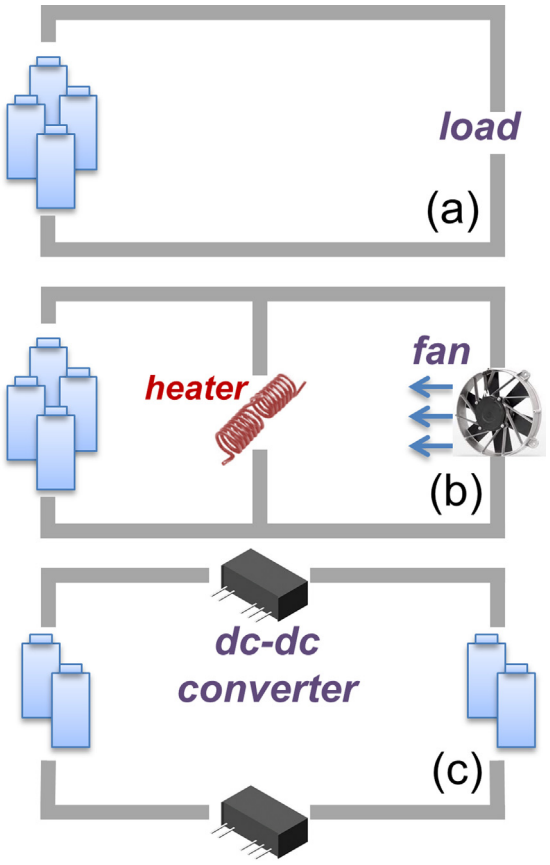

Fig. 1. Heating strategies using battery power (a) self-internal heating, (b) convective heating, and (c) mutual pulse heating.

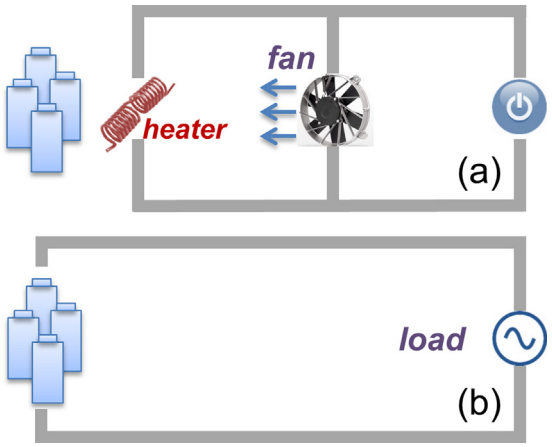

Fig. 2. Heating strategies using external power (a) external convective heating and (b) AC heating.

avoided in this situation even at low cell SOC in order to prevent Li plating. Two operation protocols are investigated here: constant current (CC) discharge and constant voltage (CV) discharge.

Simulation of the heating process is performed by discharging the cell at different CC rates and CV levels until it reaches 20 °C. The evolution of voltage (CC mode), current (CV mode) and temperature of the cell are plotted in Fig. 3. For either protocol, the heating time can be significantly reduced by using higher current (Fig. 3(a)) or lower voltage level (Fig. 3(b)), due to increased heat generation. The maximum heating rate is limited by lithium ion transport in solid phase and electrolyte. Also observed is a transitional period during which the cell voltage (CC mode) or current (CV mode) decreases first before the subsequent rise. The initial decrease in cell performance is somewhat counterintuitive because the cell is getting warmer. In fact, there is an initial period when electrolyte concentration polarization gradually builds up. The increase in ionic resistance due to departures from the optimal concentration where maximum ionic conductivity is reached counteracts the ionic conductivity increase owing to temperature rise. The CC discharge and CV discharge protocols induce different shapes of temperature evolution profiles that are concave upward for CV mode and concave downward for CC mode. Rate of temperature rise achieves its maximum early for CC discharge, but continues to increase for CV discharge.

To understand the effect of discharge protocols on solid phase diffusion, a parameter, *iSOC*, is introduced to reflect the dimensionless stoichiometry on the solid particle interface, i.e.:

$$iSOC = \begin{cases} \dfrac{c_{s,i}}{c_{s,\max}} & \text{(anode)} \\ 1 - \dfrac{c_{s,i}}{c_{s,\max}} & \text{(cathode)} \end{cases} \quad (1)$$

where $c_{s,i}$ is concentration of lithium on solid particle interface, $c_{s,\max}$ is the maximum concentration of lithium in solid phase. The *iSOC* next to the separator is plotted as a function of time, as

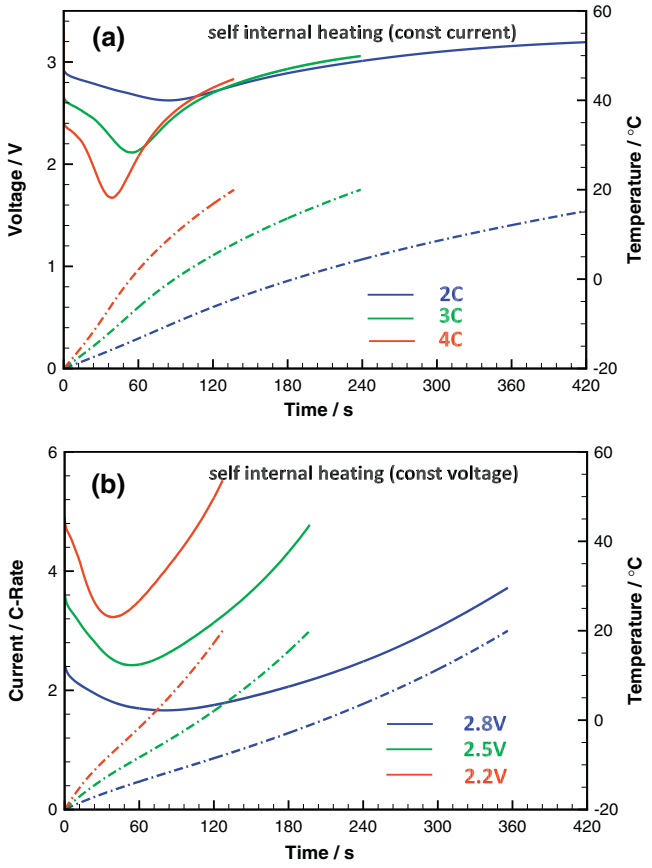

Fig. 3. Voltage, current and temperature evolution during self-internal heating (a) constant current discharge and (b) constant voltage discharge.

shown in Fig. 4. CC discharge at 4 C rate and CV discharge at 2.2 V are selected to compare because they generate very close heating times. The *iSOC* decreases for both of the two protocols at the beginning. After that, the *iSOC* for CV protocol remains constant (around 0.01) during the rest of discharge. For CC protocol, however, the *iSOC* drops to even lower level (0.002), though rising later. Unstable *iSOC* may lead to cell shut down due to solid-state diffusion limitation. The CV protocol outperforms CC protocol in that it is able to maintain *iSOC* at a stable level.

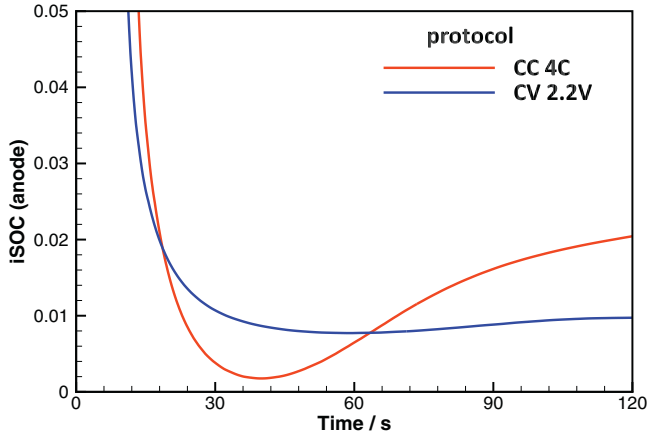

Fig. 4. Effect of discharge protocol on particle *iSOC*.

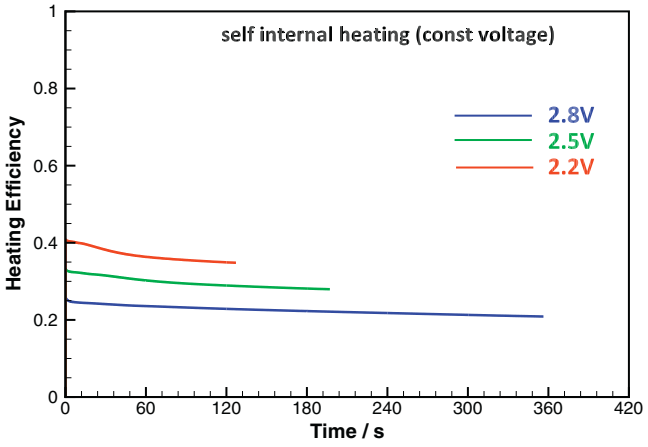

Fig. 5. Efficiency of self-internal heating.

To evaluate the percentage of consumed power used for cell warmup, a heating efficiency is defined as:

$$\eta = \frac{c_p m_C \, dT_C/dt}{\dot{q}_C + P_{out}} \tag{2}$$

where $\dot{q}_C$ is cell internal heat generation rate, P_{out} is cell output power to the external circuit. By using this definition, the heating efficiency is calculated at each time instant and shown in Fig. 5. The heating efficiency for self-internal heating is no higher than 50% at all voltage levels. The low heating efficiency is expected as cell output power is not converted to heat. Larger heating efficiency is obtained at lower voltage levels where more electrical energy is used for internal resistive heating.

The self-internal heating strategy does not require additional heat transfer system nor circuit components, which enables low cost and high reliability. However, this strategy suffers low heating efficiency and thus extra battery capacity loss. It also requires longer time compared to the other strategies to be discussed in the following sections.

3.1.2. Convective heating

Convective heating strategy heats the cell both internally and externally. The external heating is achieved using cell output power, through a resist heater and a fan simultaneously, as shown in Fig. 1(b). The heater converts electric power to heat, and the fan creates a convective flow that enhances heat transfer from heater to fluid (i.e. air here) and then from fluid to cell.

The convective heating of the cell requires a closed system enclosing flow channel, heater, fan, cell and other control components, as shown schematically in Fig. 6. For simplicity, cell, heater and fluid are assumed to have uniform temperature distribution in

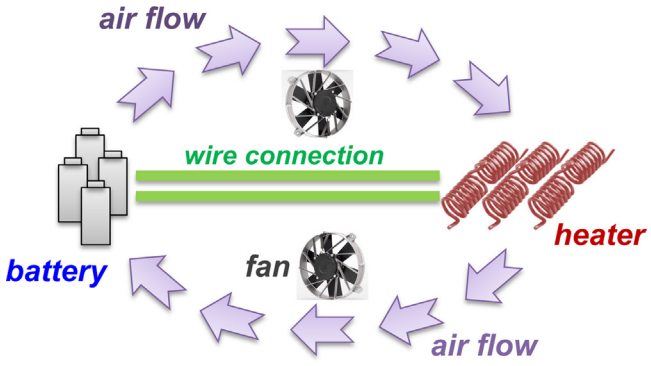

Fig. 6. Schematic view of convective heating system.

Table 3
Heat transfer properties of convective heating system.

Component	Mass (g)	c_p (J kg^{-1} K^{-1})	h (W m^{-2} K^{-1})
Cell	44	823	214
Heater	2.2	390	245
Air	0.034	1005	–

each of them. Lumped thermal equations are employed to evaluate their temperatures:

$$m_C c_{pC} \frac{dT_C}{dt} + h_C A_C (T_C - T_A) = \dot{q}_C \quad (3)$$

$$m_H c_{pH} \frac{dT_H}{dt} + h_H A_H (T_H - T_A) = I^2 R_H \quad (4)$$

$$m_A c_{pA} \frac{dT_A}{dt} + h_C A_C (T_A - T_C) + h_H A_H (T_A - T_H) = 0 \quad (5)$$

Here m, c_p, T, t, h represents mass, specific heat, temperature, time and convective heat transfer coefficient, respectively. Subscripts C, H, A stand for cell, heater and air respectively. I is the current going through the heater and R_H is the heater resistance. $\dot{q}_C$ is cell internal heat generation rate, calculated by the electrochemical–thermal coupled model using Eq. (21).

The fluid used for convective heat transfer can be air or liquid. Liquid provides better thermal conductivity and higher convective heat transfer rate, but puts a more stringent requirement on the heating system. The pros and cons of each fluid medium are outside of the scope of this paper and will not be discussed here.

In the present work, air is used as heat transfer media. The air flows along the axial direction of the 18650 cells and therefore circular-tube annulus flow is assumed between channel wall and lateral surface of the cell. The convective heat transfer coefficient and friction factor on the cell surface are evaluated using empirical relations for circular-tube annulus flow. The flow regime can be either laminar or turbulent depending on the mass flow rate of air and channel size. As for air flow around the heater, due to the small wire diameter of the heater coil, the flow is treated as if it is flowing past an infinite cylinder. Parameter study of this convective heating system under different air mass flow rates and channel-cell distances has been performed. It is found that, compared to laminar flow, turbulent flow provides a little lower h_C but much larger h_H at the same amount of fan power consumption (or flow head loss). The turbulent flow regime is the preferred choice for heat transfer in the present heating system. The present study uses a gap of 2.20 mm between channel wall and cell surface, and air mass flow rate of 2.34 g s^{-1} in the channel. Relevant heat transfer parameters are listed in Table 3.

In modeling the convective heating, cells are operated under mixed protocol of power and resistance discharge. A small portion of cell output power is used to compensate the head loss of the air flow. For simplicity, only head loss around the cell is accounted for, which is equivalent to 3 W power consumption based on head loss analysis. The rest of cell output power is supplied to the heater, whose resistance can be controlled by changing the heater coil length. In the present study, heater resistances of 0.4 Ω, 0.6 Ω and 0.8 Ω are simulated.

The convective heating process starts at −20 °C and continues until the temperature of the cell rises to 20 °C. Cell voltage (solid line) and temperature (dashed line) evolution are plotted in Fig. 7(a). The voltage decreases somewhat in the first 12 s and continues to increase during the rest of the heating process because of rate boost induced by temperature rise. Shorter heating time is achieved with lower heater resistance due to higher heating power both internally (larger voltage drop) and externally (larger current). The heating time reduces from 201 s to 85 s with the

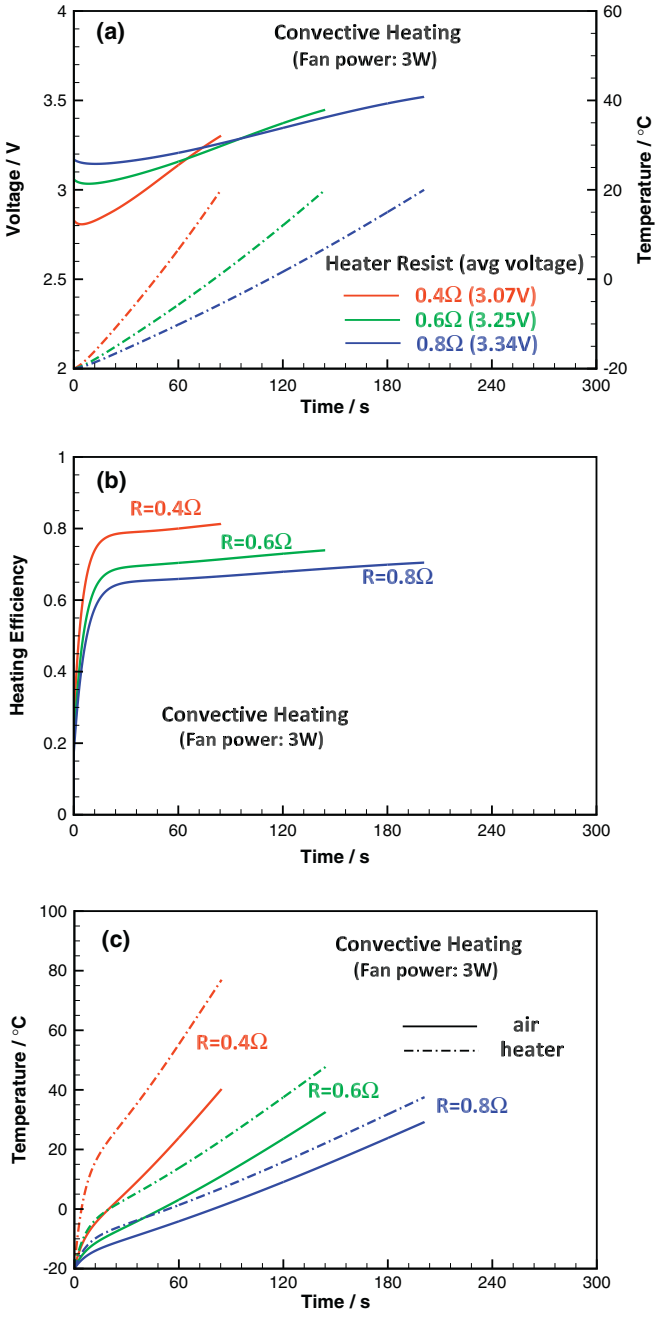

Fig. 7. Evolutions of (a) cell voltage and temperature, (b) heating efficiency, and (c) air and heater temperature in convective heating.

decrease of heater resistance from 0.8 Ω to 0.4 Ω. Compared to self-internal heating, which takes 2 min while maintaining the cell at 2.2 V voltage level, the convective heating is more efficient because of reduced heating time (close to 1 min) achieved at a relatively higher cell voltage (3.07 V on average).

The heating efficiency defined by Eq. (2) is plotted in Fig. 7(b). It ranges between 0.6 and 0.8 during most of the heating time, much higher than observed in self-internal heating. The heating efficiency is higher at lower heater resistance because of larger heating power while constant head loss is maintained. Initially, the heating efficiency exhibits a transition period, marked by a sharp increase after beginning at very low level. The low level of initial heating efficiency is due to the energy consumed for temperature increase in both heater and air, which should be warmed up prior to transfer of heat to the cell. Fortunately, the air mass is relatively

small and low specific heat materials can be used as heater coil, helping to minimize energy and time required to warm up both air and heater. However, for the battery pack system in an EV, more inertial components are expected for control and safety reasons. The thermal mass of these components should be minimized to ensure high heating efficiency.

The evolutions of heater and air temperature are shown in Fig. 7(c). Higher temperature of air and heater, as well as larger temperature difference between air and heater, are observed at smaller heater resistance. This is because at high heating rate, the convective heat transfer between components becomes rate-limiting for heat transfer. More attention should be paid during rapid heating in case air and heater temperature exceeds the threshold level for safety concerns.

The advantage of convective heating strategy lies in its higher efficiency and thus shorter time, owing to full utilization of cell's output power. However, this strategy suffers from several disadvantages. First, the convective heating requires a flow loop and a fan for air circulation, increasing cost, system complexity, and reducing system reliability. Second, heat transfer from air to the cell becomes more difficult for larger cells, where heat conduction inside cells is more rate-limiting due to longer heat conduction distance and induces larger temperature gradient inside cells. Last, the head loss of flow and the heating of inertial components consume additional energy, which may significantly reduce the heating efficiency in complex systems where more inertial components exist.

3.1.3. Mutual pulse heating

In this section we study a strategy that utilizes cell output power and at the same time heats the cell internally, namely to allow the cells to charge or discharge themselves. Practically, the cells in a whole battery pack are divided into two groups with equal capacity. Whenever one group is discharging, the other group is charging. The output power of the discharge group is used as the input power of the charge group. Since voltage required to charge cells is higher than cell output voltage, a dc–dc converter is needed to boost cell's discharge voltage. To balance the capacity of the two groups, the charge/discharge roles of the two groups switch at intervals of a period, accomplished by using pulse signals. Accordingly, this strategy is named mutual pulse heating, as schematically shown in Fig. 1(c). In the present study for simplicity, each cell group is represented by a single cell.

The mutual pulse heating strategy successfully fulfills the requirement that cell output power is used for internal heating, although this at first seems paradoxical. In this way, a portion of output power of the discharging cell is used to heat the charging cell through its internal resistance. The rest of the output power is stored in the charging cell and will be available to use during the next pulse interval. The heating efficiency of the system is defined as the ratio of the internal thermal energy gain to the total power consumption of the whole battery pack. In our simplified two-cell system, the heating efficiency is defined as:

$$\eta_H = \frac{c_{p1} m_1 \, dT_1/dt + c_{p2} m_2 \, dT_2/dt}{\dot{q}_1 + \dot{q}_2 + P_{out} + P_{in}} \tag{6}$$

where $\dot{q}_1$ and $\dot{q}_2$ are internal heat generation rate of the two cells. P_{in} and P_{out} represents input power of the charging cell and output power of the discharging cell, respectively. They are related by:

$$P_{in} = -P_{out} \eta_{dc} \tag{7}$$

Here η_{dc} is the efficiency of the dc–dc converter.

Modeling of the mutual pulse heating requires the simulation of two cells simultaneously. The two cells are set to start with the same initial conditions. The discharging cell is under constant voltage protocol while the charging cell is under designated power protocol described by Eq. (7). The voltage and temperature evolutions

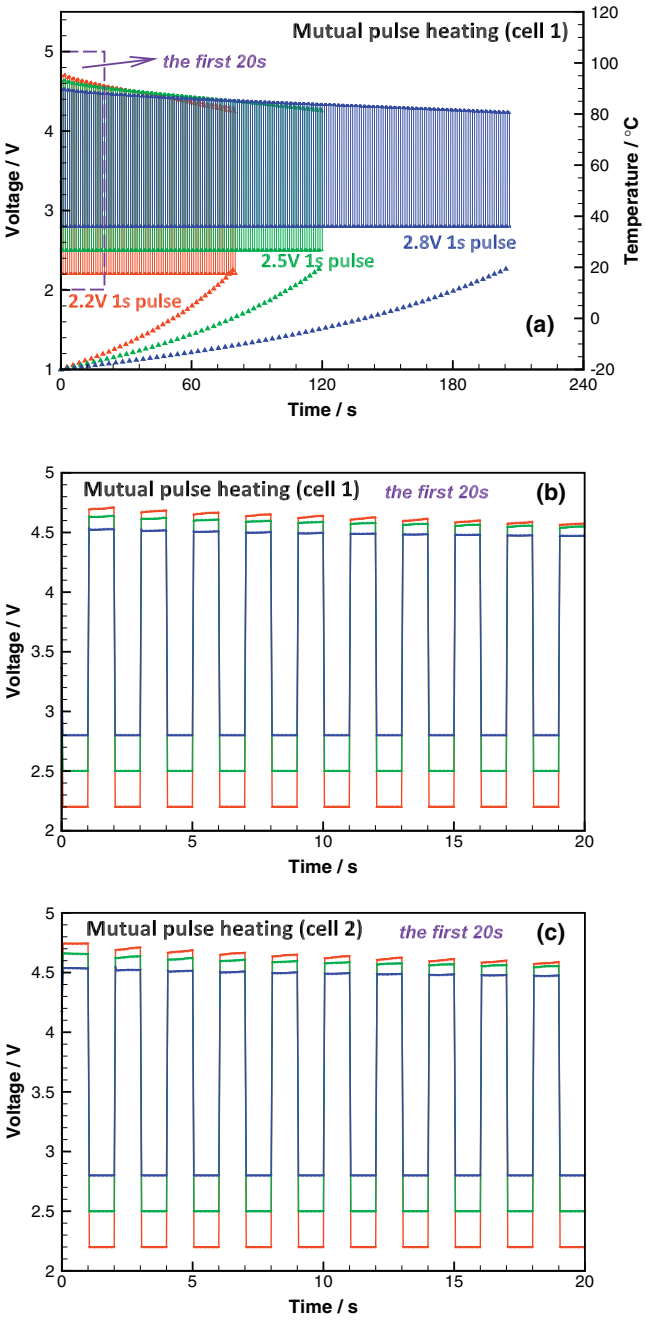

Fig. 8. Voltage and temperature evolution during mutual pulse heating (a) the entire heating process, (b) the first 20 s for cell1, and (c) the first 20 s for cell 2.

of cell 1 during the entire heating process are shown in Fig. 8(a). Discharge voltage levels of 2.2 V, 2.5 V and 2.8 V are modeled independently. Again, lower levels of discharge voltage exhibit shorter heating time because of higher internal resist heating power. The pulse intervals are tentatively set to 1 s. The voltage evolution profiles during the first 20 s are magnified, as shown in Fig. 8(b) for cell 1 and Fig. 8(c) for cell 2. The lowest discharge voltage level (2.2 V), however, yields the highest charging voltage, owing to much larger discharge current and thus higher output power.

The charging voltage may be higher than 4.5 V, giving rise to the possibility of Li plating. To examine this issue further, the lithium ion concentration on the graphite particle surface, defined as dimensionless *iSOC*, is monitored. Fig. 9 shows the *iSOC* variation range during the first pulse cycle of cell 2, which has first been charged for 1 s and discharged for another 1 s. The maximum

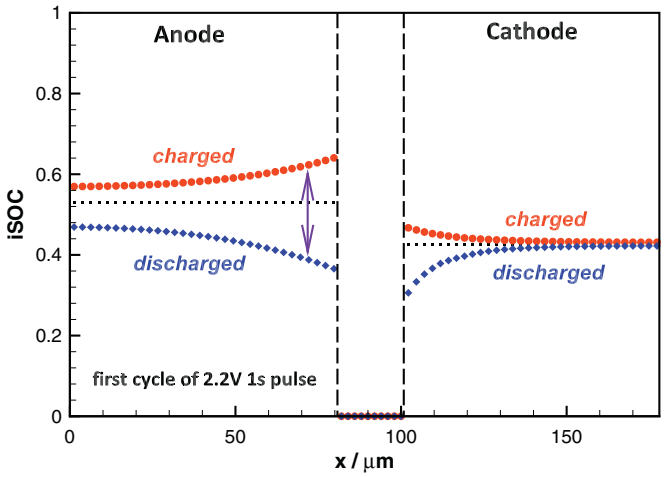

Fig. 9. *iSOC* evolution during mutual pulse heating.

iSOC in the graphite anode appears at the anode-separator interface and reaches 0.64 at the end of the charge interval, indicating safe operation free of Li plating. Fig. 9 reveals that, the anode-separator interface has the largest *iSOC* variations, which originates from the relatively lower conductivity of the electrolyte compared to the solid matrix, because it is also the location where the local reaction current reaches maximum. Small *iSOC* variations are preferred since large variation may induce partially overcharge or overdischarge of the active material. This prompts us to investigate the pulse frequency effect, because higher frequency pulses generate smaller *iSOC* variations due to insufficient time for solid-phase concentration buildup.

Mutual pulse heating is simulated for three different pulse intervals (0.1 s, 1 s and 10 s). The starting cell voltage has been increased from 3.8 V to 4.0 V in order to evaluate the possibility of Li plating at high SOC. Discharge voltage is kept at 2.5 V. The *iSOC* at the anode-separator interface is plotted as a function of time in Fig. 10. The *iSOC* from 10 s interval pulse shows extremely large variations, rising and falling across most of the stoich range. Moreover, it rises and approaches the unity during the first charging interval, implying high risk of Li plating. The *iSOC* variations from 1 s and 0.1 s interval pulses are much smaller. Furthermore, the highest *iSOC* for the latter two cases is well below 0.9, less likely to incur Li plating. Physically, high frequency pulse signal implies rapid switches between charge–discharge mode, preventing solid-phase concentration buildup, leading to smaller *iSOC* variations.

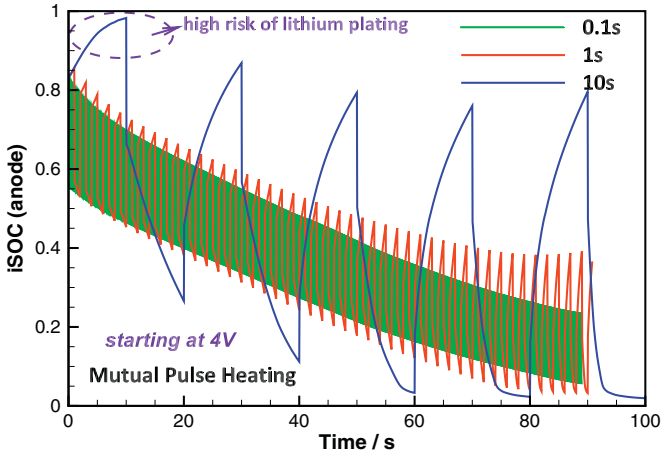

Fig. 10. *iSOC* evolution under different pulse intervals.

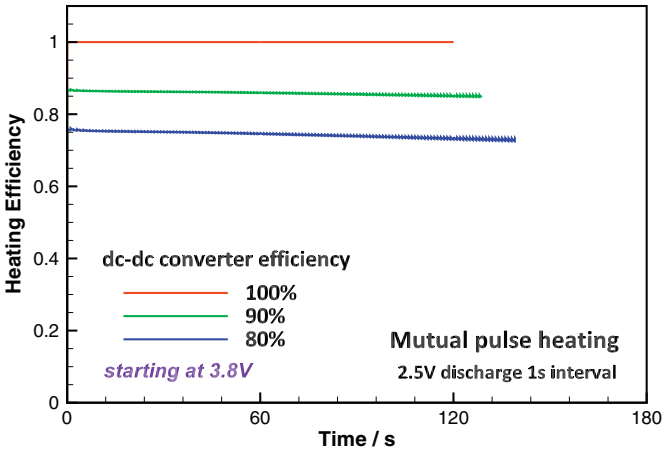

Fig. 11. Heating efficiency evolution during mutual pulse heating.

The previous calculations assume 100% dc–dc converter efficiency, an ideal case and may not be achieved for real dc–dc converters. One concern is whether system heating efficiency suffers substantial loss from reduced converter efficiencies. To answer this question, the heating efficiency evolutions at three converter efficiency levels are calculated, as shown in Fig. 11. The system heating efficiencies are only slightly lower than the converter efficiency, ranging from 0.85 to 0.86 for 90% converter efficiency and from 0.75 to 0.73 for 80% converter efficiency. To achieve high energy utilization, high efficiency converters are preferred.

The mutual pulse heating method has three major advantages. First, it provides a heating system with low maintenance and high reliability due to lack of any moving parts, and without the need of convective heat transfer system. Second, cell internal temperature distribution is nearly uniform because the system is free of external heating. Last, high energy utilization and short heating time can be achieved by using high efficiency dc–dc converters and low discharge voltages. However, disadvantages also exist. The mutual pulse operation requires a specially designed circuit and control system, which increases cost. Moreover, pulse heating at high SOC should be used cautiously in consideration of Li plating. High frequency pulsing is a good innovation to reduce this risk.

3.1.4. Comparison

Three heating strategies using battery power have been introduced and modeled, each with its own advantages and disadvantages. It is instructive to compare these strategies in terms of the four criteria described in Section 1.

Heating study cases for the aforementioned three strategies are plotted in Fig. 12 in terms of heating time and cell capacity loss. Each case is represented by one symbol. The voltage number labeled above each symbol is an indication of the discharge voltage level. For mutual pulse heating and self-internal heating, where constant voltage protocols are employed, the voltage number is the actual discharge cell voltage level. For convective heating where cell voltage changes with time, the labeled number is the average cell voltage over the heating period. Strong sensitivity of heating time to voltage level indicates that heating time can be significantly reduced by employing lower voltage levels during discharge as long as the cell works properly without damage induced and significant degradation. In addition, these voltage numbers are also served for heating time comparison. Heating time of different strategies should be compared under the same discharge voltage level.

If decreased battery capacity is the primary concern of manufacturers, mutual pulse heating with high efficiency dc–dc converters is the best option. The minimum capacity consumed to warm up cells from −20 °C to 20 °C can be as low as 5% of the cell capacity. For

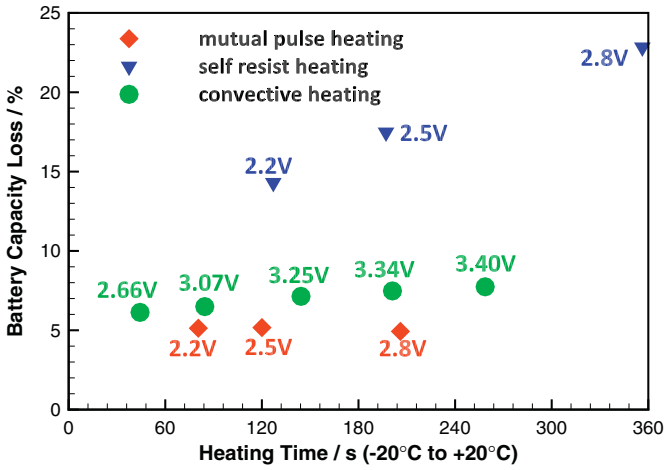

Fig. 12. Comparison of heating strategies using battery power.

the Nissan Leaf with maximum driving range of 138 miles at ideal condition, energy used for mutual pulse heating consumes only 7 miles of driving range. This would be a dramatic improvement from the current loss of 75 miles in −10 °C cold weather.

If the primary consideration is to reduce heating time, convective heating is the preferred choice. At 2.5 V discharge voltage level, it takes 197 s for self-internal heating, and 120 s for mutual pulse heating to warm up the cell from −20 °C to 20 °C. The convective heating spends much less time (44 s) to achieve that goal with slightly higher voltage level (2.66 V). Convective heating is the fastest because most of the power generated from the battery is converted to heat, both internally and externally. The mutual pulse heating, though featuring a high heating efficiency, has output power partially converted to chemical energy stored in the battery without heat generation, limiting its heat generation rate.

For a battery pack composed of large-size cells, convective heating should be used with caution. Because of longer distance for heat conduction inside cells, a large temperature gradient might develop internally, leading to higher cell surface temperature and reduced convective heat transfer rate.

The above study compares four heating strategies in terms of battery capacity loss and heating time. The remaining two criteria, system cost and durability, which cannot be quantified by our model, are equally important for manufacture of the heating system. In terms of system cost, the self-internal heating provides a low-cost option due to its simplicity. The convective heat transfer system in convective heating and dc–dc converter in mutual pulse heating add additional cost. System durability is reflected in the need for maintenance of the mechanical system, as well as cycle life of the battery pack. Mutual pulse heating possesses an advantage over the convective heating system by offering low maintenance and high reliability since the latter suffers from possible damage of moving parts in its air circulation system. As for battery cycle life, it is affected by charge–discharge protocols employed in different heating strategies. A more comprehensive model incorporating degradation effects is needed to investigate the influences of heating strategies on battery cycle life, which is our future work.

3.2. Heating strategies using external power

In the above section, heating power comes completely from the battery pack, which is the only onboard power source in EVs. When customers have access to external power, such as home charging using household electric power, the heating power can be extracted externally. In this situation, battery capacity consumption is no longer considered an essential criterion for evaluation. However, the other three criteria are still valid here, namely, heating time, system cost and system durability.

Regarding heating strategies using external power, self-internal heating and mutual pulse heating strategies are not practical since they rely exclusively on battery power. The convective heating can be modified by connecting the heater and fan to the external power source without extracting power from the battery, which is termed as external convective heating, as shown in Fig. 2(a). This is actually a heat transfer problem without electrochemical reactions, and thus will not be addressed in the present study. However, it is easy to infer that external convective heating is not a good option for large cells, due to possible large temperature difference inside cells, as is analyzed in the convective heating section.

Internal heating is a preferred method in that it heats the cell uniformly and induces little temperature difference inside cells. At the same time, the cell needs to be charged and discharged periodically to avoid any change in cell SOC. From this point of view, alternating current is a good option since it not only satisfies the above requirement but also is easily accessed household electricity. This strategy is named AC heating as shown in Fig. 2(b).

3.2.1. AC heating

AC signals are described by two parameters: amplitude and frequency. To minimize the heating time, large amplitude signals are desired. Caution should be exercised when using high power heating in case that maximum power limitation is exceeded.

The signal frequency is an essential parameter that affects fundamental kinetic and transport processes of Li-ion cells. To analyze its effect, electrochemical impedance spectroscopy (EIS) is simulated by using small amplitude AC signal as input using the present ECT model. Double layer effect at reaction interface is incorporated by using the following equations:

$$i = i_{DL} + i_F \tag{8}$$

$$i_{DL} = C_{DL}\frac{\partial(\phi_s - \phi_e)}{\partial t} \tag{9}$$

where i_{DL} is the double layer current density, i_F is the faradic (reaction) current density as expressed by Eq. (16). C_{DL} is the double layer capacitance(0.2 F m^{-2} is used in the present study). The double layer current is zero for DC signal, negligible for low frequency signal, but takes a significant portion of the total current for high frequency signal.

A sinusoidal voltage signal of 5 mV magnitude is used as input to the cell. The current response is monitored for multiple cycles until a stable phase shift is obtained. A time step of 1/10 signal period would be enough for high frequency signals, but needs to drop to 1/100 period or even smaller for low frequency signals. The impedance is then represented as a complex number whose absolute value is the magnitude ratio of voltage and current, and whose argument is the opposite value of current phase shift. A wide range of frequency from 10^{-5} to 10^{7} Hz has been simulated at three ambient temperatures (25 °C, 0 °C, and −20 °C) and the results are plotted in Fig. 13, consisting of a Nyquist plot (a) and two Bode plots (b) and (c).

The EIS data exhibits three major trends. First, reducing temperature induces large impedance rise for all frequencies, especially in the mid-range frequency region, as represented by semi-circle diameter in Fig. 13(a). The observation coincides with the present understanding of Li-ion cell behavior at low temperature as discussed in Section 1.

Second, the magnitude of impedance decreases with increasing frequency, as shown in Fig. 13(b). As the frequency rises, two sharp drops in impedance emerge in two separate frequency regions. The first drop appears in low frequency (10^{-5} to 10^{-3} Hz) region,

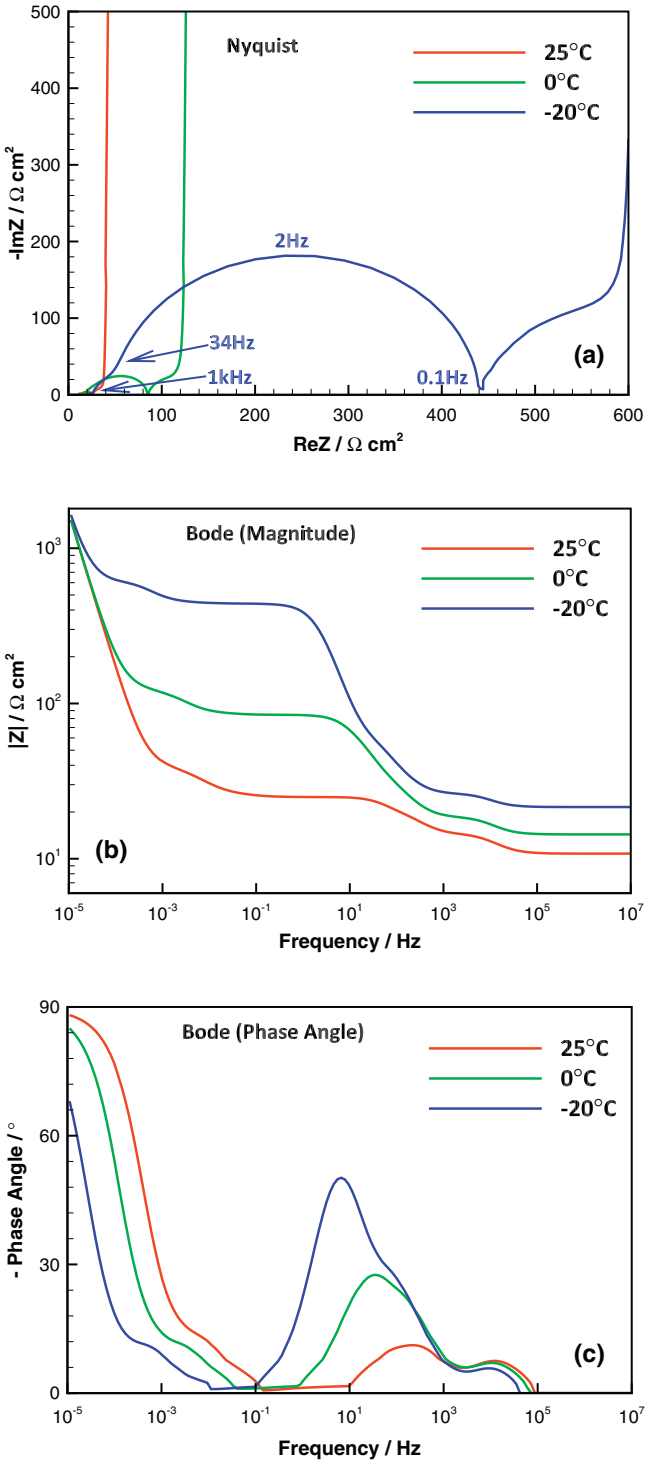

Fig. 13. Model predicted EIS data (a) Nyquist plot, (b) Bode plot of magnitude, and (c) Bode plot of phase angle.

accompanied by the sharp decrease of phase angle (from 90° to 0°). The diffusion processes in electrolyte and solid phase dominates at low frequency because of their relatively larger time constant. Above this frequency level, alternating current direction switches so fast that the buildup of concentration gradient could not happen. The second drop appears in mid frequency (10^0 to 10^2) region, where phase angle rises at first and then drops to zero. In this region, the current going through the double layer keeps increasing because of reduced capacitor impedance. Above this frequency level, the current produced from faradic process (charge transfer at particle–electrolyte interface) is gradually bypassed by the current going through the double layer. The impedance gradually decreases and eventually becomes constant, i.e. the high frequency resistance. In other words, at very high frequency, the cell acts as a pure resistor, where both diffusional and kinetic processes are bypassed.

Third, temperature affects the critical frequency where impedance transition occurs. The critical frequency decreases with reducing temperatures. For instance, as shown in Fig. 13(b) and (c), the impedance drop in mid-frequency region starts at 10 Hz at 25 °C, 1 Hz at 0 °C and 0.1 Hz at −20 °C. This implies the ability to reduce the impedance in cold weather without requiring use of very high signal frequency.

In summary, the second trend implies that possible benefits can be derived from high frequency signal. At the same cell output voltage, high frequency signal generates higher heating power and thus less heating time due to reduced cell impedance. Additionally, more current going through the double layer suggests the possibility of extended cycle life because of reduced faraday current or lithium intercalation–deintercalation rate. The third trend tells us that these benefits can be possibly implemented at a relative lower AC frequency in cold weather condition. All these facts suggest household electricity may be a good option for AC heating, combining easy accessibility and a frequency of 60 Hz which might be sufficient to trigger these benefits at low temperatures.

To model the AC heating process, voltage signal $V(t) = 3.8 - \cos(2\pi ft)$ has been used as a protocol for Li-ion cells starting at −20 °C. Signal frequencies f of 0.01 Hz, 0.1 Hz, 1 Hz, 60 Hz and 1000 Hz are simulated respectively. Modeling high frequency AC heating presents a great computational challenge, due to very high time resolution, though possible compromises on solution accuracy can be made. In the present study, time intervals are chosen as 1/512 signal period for 0.01 Hz, 1/64 for 0.1 Hz, 1 Hz, 60 Hz, and 1/8 for 1000 Hz.

Fig. 14(a) exhibits the voltage and current evolution during the first six cycles of 60 Hz AC signal. Voltage signal is displayed by dashed black lines and current by solid lines (red for faradic current, blue for double layer current). A positive phase shift of approximately 30° is observed for double layer current due to capacitive effects. The faradic current with a peak of 1.7 A is significantly smaller than double layer current which peaks at 12.7 A. The faradic C-rate is only approximately 1/8 of the total C-rate, implying reduced cell degradation can be achieved because of much lower faradic current.

The frequency effect on heating time is reflected in Fig. 14(b), which shows the temperature evolution profiles using various AC signal frequencies. With increasing signal frequencies, the heating time decreases from 340 s at 0.01 Hz, 170 s at 60 Hz to 80 s at 1000 Hz, indicating that significant amount of heating time can be saved by using high frequency signal. As discussed in Fig. 13, the reduced heating time is a result of the decreased cell impedance at higher frequency, because of larger heating power according to $P = \Delta V^2/R$. Heating time reduction has been achieved in two frequency regions: 0.01–0.1 Hz and 1–1000 Hz. Diffusion effect is bypassed in the former region while charge transfer kinetics is gradually bypassed in the latter region. Little change in heating time is observed between 0.1 Hz and 1 Hz, where cell impedance does not change much.

Overall, the AC heating strategy provides a fast way of heating a battery pack uniformly using external power. Household electricity can be used at its original frequency (60 Hz) and provides approximately 50% time saving compared to low frequency signals. In addition, the high frequency heating benefits cycle life because of reduced faradic current. Moreover, this strategy has potential application in hybrid electric vehicles (HEVs), where onboard power can

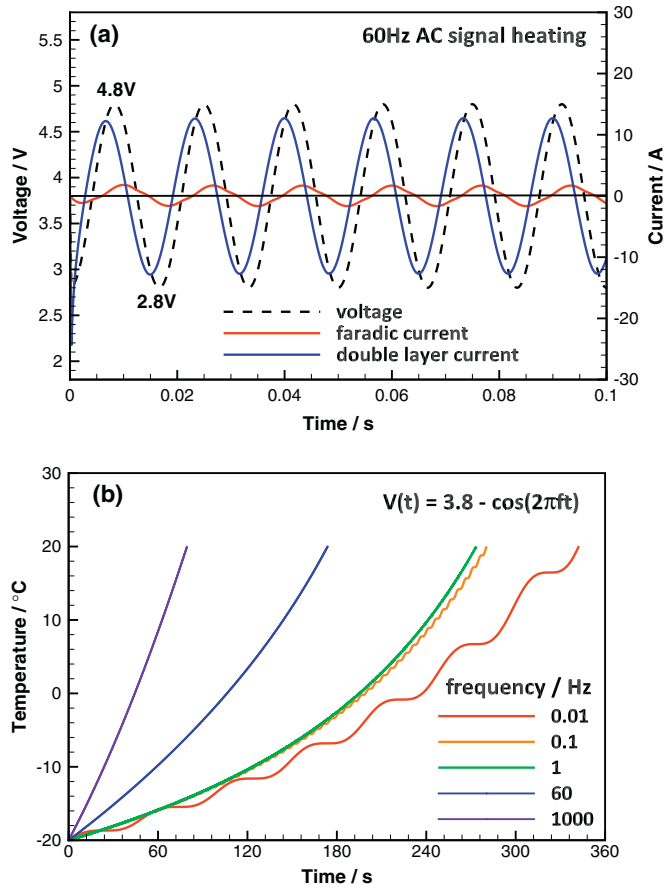

Fig. 14. Voltage, current and temperature evolution during AC heating (a) voltage and current evolution at 60 Hz and (b) temperature evolution at various frequencies.

be extracted from internal combustion engine and alternator. More experimental research on AC heating is desired to fully understand its advantages and disadvantages.

4. Conclusions

Heating of Li-ion cells from sub-zero temperatures has been studied by employing an electrochemical–thermal coupled model, which is validated against 2.2 Ah 18650 cells from −20 °C to 60 °C up to 4.6 C rate. Four strategies, namely self-internal heating, convective heating, mutual pulse heating, and AC heating using external power, are proposed and simulated and compared in the present study. Four heating criteria have been introduced and used to evaluate these strategies.

For battery power heating, convective heating requires the least heating time, while mutual pulse heating consumes the least battery capacity. Mutual pulse heating has the additional advantage of uniform internal heating and is free of convective heat transfer system.

For external power heating, AC heating is proposed because it is an internal heating strategy that provides uniform heat. Moreover, household electric power can be used at its original frequency, providing an easily accessible power source, reduced heating time and extended cycle life. It also has potential onboard application in hybrid electric vehicles (HEVs).

The present study suggests that, for either strategy, heating time can be significantly shortened by reducing cell output voltage. The capacity loss can be as little as 5% of total cell capacity for high efficiency heating. There is still considerable potential to reduce heating time and to improve driving range of EVs operated at sub-zero temperatures.

The present model is able to present quantitative prediction of heating time and capacity loss. In future studies, a degradation model will be incorporated so that the effect of heating strategy on battery cycle life can be quantified. Experimental validation of the proposed heating strategies is also suggested.

Acknowledgments

Financial support from The US Department of Energy CAEBAT Program (via National Renewable Energy Laboratory) and use of AutoLion™ software developed by EC Power are greatly acknowledged.

Appendix A. Appendix: governing equations

Applying the fully coupled electrochemical–thermal model of Gu and Wang [16], the following conservation equations are solved:

Charge conservation in solid electrodes:

$$\nabla \cdot (\sigma_s^{eff} \nabla \phi_s) - j = 0 \tag{10}$$

Charge conservation in electrolyte:

$$\nabla \cdot (\kappa^{eff} \nabla \phi_e + \kappa_D^{eff} \nabla \ln c_e) + j = 0 \tag{11}$$

in which the effective diffusional ionic conductivity:

$$\kappa_D^{eff} = \frac{2RT\kappa^{eff}}{F}(t^+ - 1)\left(1 + \frac{d \ln f_\pm}{d \ln c_e}\right) \tag{12}$$

Material conservation in electrolyte:

$$\varepsilon \frac{\partial c_e}{\partial t} = \nabla \cdot (D_e^{eff} \nabla c_e) + \frac{1 - t_+}{F} j \tag{13}$$

Material conservation in solid particles:

$$\frac{\partial c_s}{\partial t} = \frac{1}{r^2}\frac{\partial}{\partial r}\left(D_s r^2 \frac{\partial c_s}{\partial r}\right) \tag{14}$$

with boundary condition on particle surface:

$$-D_{s,i}\frac{\partial c_{s,i}}{\partial r}\bigg|_{r=R_i} = \frac{i}{F} \tag{15}$$

Butler–Volmer equation for charge transfer kinetics:

$$i = i_0\left[\exp\left(\frac{\alpha_a F}{RT}\eta\right) - \exp\left(-\frac{\alpha_c F}{RT}\eta\right)\right] \tag{16}$$

in which the kinetic overpotential:

$$\eta = \phi_s - \phi_e - U_i(c_{s,i}) - iR_f \tag{17}$$

and exchange current density:

$$i_0 = k(T) c_{s,i}^{\alpha_c} c_e^{\alpha_a} (c_{s,\max} - c_{s,i})^{\alpha_a} \tag{18}$$

Mapping between reaction current density on particle surface and volumetric current density in the electrodes:

$$j = ai \tag{19}$$

Energy conservation of the whole cell (lumped thermal model):

$$mc_p \frac{dT}{dt} = \dot{Q} + hA_s(T_\infty - T) \tag{20}$$

where h is the convective heat transfer coefficient, A_s is the cell surface area, $hA_s(T_\infty - T)$ is the convective heat. The heat generation

power:

$$\dot{Q} = A_e \int_0^L j(\phi_s - \phi_e - U) + j\left(T\frac{dU}{dT}\right) + \sigma_s^{eff}\nabla\phi_s \cdot \nabla\phi_s + \kappa^{eff}\nabla\phi_e \cdot \nabla\phi_e + \kappa_D^{eff}\nabla \ln c_e \cdot \nabla\phi_e \, dx \quad (21)$$

in which L is the sum of the anode, separator and cathode thicknesses, A_e is the electrode area, $j(\phi_s - \phi_e - U)$ represents kinetic heat, $j(T(dU/dT))$ is the reversible heat, $\sigma_s^{eff}\nabla\phi_s \cdot \nabla\phi_s$, $\kappa^{eff}\nabla\phi_e \cdot \nabla\phi_e$ and $\kappa_D^{eff}\nabla \ln c_e \cdot \nabla\phi_e$ are joule heat from electronic resistance, ionic resistance and concentration overpotential respectively.

References

[1] NissanUSA, How conditions affect range, 2012. http://www.nissanusa.com/leaf-electric-car/range?next=ev_micro.section_nav
[2] G. Nagasubramanian, Electrical characteristics of 18650 Li-ion cells at low temperatures, Journal of Applied Electrochemistry 31 (2001) 99.
[3] S.S. Zhang, K. Xu, T.R. Jow, Electrochemical impedance study on the low temperature of Li-ion batteries, Electrochimica Acta 49 (2004) 1057.
[4] H.P. Lin, D. Chua, M. Salomon, H.C. Shiao, M. Hendrickson, E. Plichta, S. Slane, Low-temperature behavior of Li-ion cells, Electrochemical and Solid-State Letters 4 (2001) A71.
[5] J. Fan, S. Tan, Studies on charging lithium-ion cells at low temperatures, Journal of the Electrochemical Society 153 (2006) A1081.
[6] C.K. Huang, J.S. Sakamoto, J. Wolfenstine, S. Surampudi, The limits of low-temperature performance of Li-ion cells, Journal of the Electrochemical Society 147 (2000) 2893.
[7] S.S. Zhang, K. Xu, T.R. Jow, The low temperature performance of Li-ion batteries, Journal of Power Sources 115 (2003) 137.
[8] M.C. Smart, B.V. Ratnakumar, S. Surampudi, Electrolytes for low-temperature lithium batteries based on ternary mixtures of aliphatic carbonates, Journal of the Electrochemical Society 146 (1999) 486.
[9] M.C. Smart, B.V. Ratnakumar, S. Surampudi, Use of organic esters as cosolvents in electrolytes for lithium-ion batteries with improved low temperature performance, Journal of the Electrochemical Society 149 (2002), A361-A370.
[10] S.S. Zhang, K. Xu, T.R. Jow, Low temperature performance of graphite electrode in Li-ion cells, Electrochimica Acta 48 (2002) 241.
[11] M.D. Zolot, K. Kelly, M. Keyser, M. Mihalic, A. Pesaran, A. Hieronymus, Thermal evaluation of the Honda insight battery pack, in: 36th Intersociety Energy Conversion Engineering Conference, Savannah, GA, 2001, p. 923.
[12] A. Pesaran, A. Vlahinos, T. Stuart, Cooling and preheating of batteries in hybrid electric vehicles, in: The 6th ASME-JSME Thermal Engineering Joint Conference, Hawaii Island, Hawaii, 2003.
[13] S.S. Zhang, K. Xu, T.R. Jow, Charge and discharge characteristics of a commercial LiCoO(2)-based 18650 Li-ion battery, Journal of Power Sources 160 (2006) 1403.
[14] A. Vlahinos, A. Pesaran, Energy efficient battery heating in cold climates, in: The Future Car Congress, Arlington, Virginia, 2002.
[15] T.A. Stuart, A. Hande, HEV battery heating using AC currents, Journal of Power Sources 129 (2004) 368.
[16] W.B. Gu, C.Y. Wang, Thermal–electrochemical modeling of battery systems, Journal of the Electrochemical Society 147 (2000) 2910.
[17] V. Srinivasan, C.Y. Wang, Analysis of electrochemical and thermal behavior of Li-ion cells, Journal of the Electrochemical Society 150 (2003) A98.
[18] G. Luo, C.Y. Wang, A. Multidimensional, Electrochemical–thermal coupled lithium-ion battery model, in: X. Yuan, H. Liu, J. Zhang (Eds.), Lithium-Ion Batteries: Advanced Materials and Technologies, CRC Press, Boca Raton, 2012, p. 303.
[19] Y. Ji, Y.C. Zhang, C.Y. Wang, Li-ion cell operation at low temperatures, Journal of the Electrochemical Society 160 (2013) A636.
[20] M. Doyle, T.F. Fuller, J. Newman, Modeling of galvanostatic charge and discharge of the lithium polymer insertion cell, Journal of the Electrochemical Society 140 (1993) 1526.
[21] T.F. Fuller, M. Doyle, J. Newman, Simulation, optimization of the dual lithium ion insertion cell, Journal of the Electrochemical Society 141 (1994) 1.
[22] M. Doyle, J. Newman, A.S. Gozdz, C.N. Schmutz, J.M. Tarascon, Comparison of modeling predictions with experimental data from plastic lithium ion cells, Journal of the Electrochemical Society 143 (1996) 1890.
[23] C. Shaffer, Development of cell/pack level models for automotive Li-ion batteries with experimental validation, in: Proc. DOE Vehicle Technologies Program Annual Merit Review and Peer Evaluation Meeting, Washington, D.C., May 14–18, 2012.
[24] T.R. Jow, M.B. Marx, J.L. Allen, Distinguishing Li^+ charge transfer kinetics at NCA/electrolyte and graphite/electrolyte interfaces, and NCA/electrolyte and LFP/electrolyte interfaces in Li-ion cells, Journal of the Electrochemical Society 159 (2012) A604.
[25] W.F. Fang, O.J. Kwon, C.Y. Wang, Electrochemical–thermal modeling of automotive Li-ion batteries and experimental validation using a three-electrode cell, International Journal of Energy Research 34 (2010) 107.
[26] K.M. Shaju, G.V.S. Rao, B.V.R. Chowdari, Influence of Li-ion kinetics in the cathodic performance of layered $Li(Ni_{1/3}Co_{1/3}Mn_{1/3})O_2$, Journal of the Electrochemical Society 151 (2004) A1324.
[27] T.L. Kulova, A.M. Skundin, E.A. Nizhnikovskii, A.V. Fesenko, Temperature effect on the lithium diffusion rate in graphite, Russian Journal of Electrochemistry 42 (2006) 259.
[28] M.W. Verbrugge, B.J. Koch, Electrochemical analysis of lithiated graphite anodes, Journal of the Electrochemical Society 150 (2003) A374.
[29] N. Yabuuchi, Y. Makimura, T. Ohzuku, Solid-state chemistry and electrochemistry of $LiCo_{1/3}Ni_{1/3}Mn_{1/3}O_2$ for advanced lithium-ion batteries III. Rechargeable capacity and cycleability, Journal of the Electrochemical Society 154 (2007) A314.
[30] Y.F. Reynier, R. Yazami, B. Fultz, Thermodynamics of lithium intercalation into graphites and disordered carbons, Journal of the Electrochemical Society 151 (2004) A422.
[31] W. Lu, I. Belharouak, D. Vissers, K. Amine, In situ thermal study of $Li_{1+x}[Ni_{1/3}Co_{1/3}Mn_{1/3}]_{(1-x)}O_2$ using isothermal micro-clorimetric techniques, Journal of the Electrochemical Society 153 (2006) A2147.
[32] L.O. Valoen, J.N. Reimers, Transport properties of $LiPF_6$-based Li-ion battery electrolytes, Journal of the Electrochemical Society 152 (2005) A882.